

Electronic supplementary information

Carbon-encapsulated ultrathin MoS₂ nanosheets epitaxially grown on porous metallic TiNb₂O₆ microspheres with unsaturated oxygen atoms for superior potassium storage

Lidong Xing,^{‡a} Qiyao Yu,^{‡a} Bo Jiang,^{‡b} Jianhua Chu,^a Cheng-Yen Lao,^c Min Wang,^a Kun Han,^a
Zhiwei Liu,^a Yanping Bao^{*a} and Wei (Alex) Wang^{*cd}

*^a State Key Laboratory of Advanced Metallurgy, University of Science and Technology Beijing,
Beijing 100083, China*

** E-mail: baoyp@ustb.edu.cn.*

*^b Department of Materials Science and Engineering, NTNU Norwegian University of Science and
Technology, Trondheim 7491, Norway*

*^c Department of Materials Science and Metallurgy, University of Cambridge, Cambridge CB3 0FS,
UK*

*^d Department of Materials Science and Engineering, College of Engineering, Peking University,
Beijing 100871, China*

** E-mail: wwangbj@pku.edu.cn.*

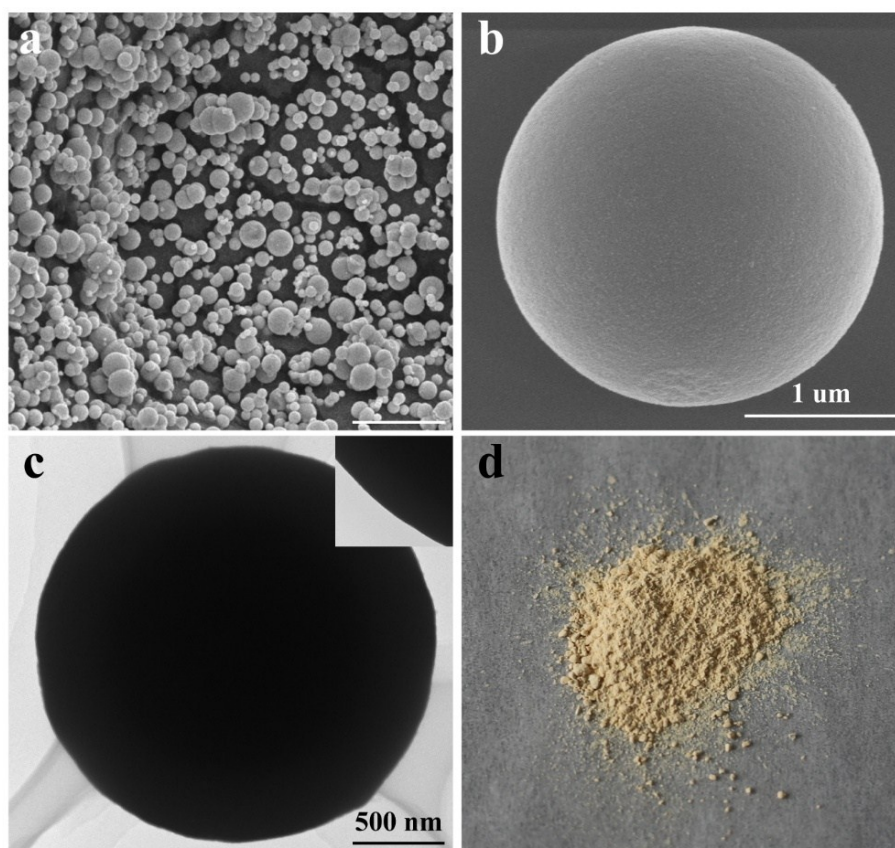


Fig. S1 (a-b) FESEM and (c) TEM images and (d) the photographs of the smooth TiNb_2O_7 microspheres before annealing.

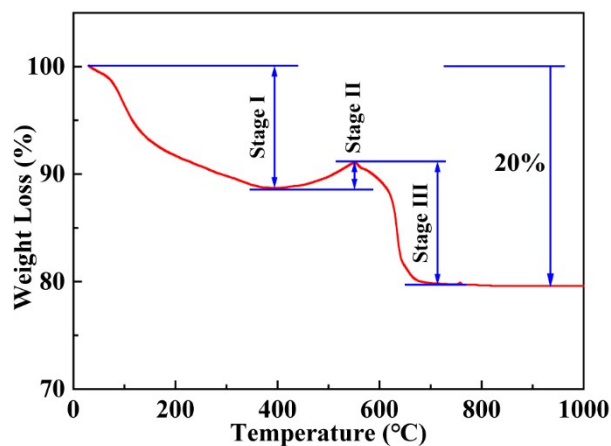


Fig. S2 TGA curve of the titanium niobium oxide microspheres with a ramp rate of 10 °C min⁻¹.

It can be seen from the TGA results that calcination can be divided into three stages. From room temperature to 400 °C is the stage I of TGA curve, and the weight loss is 11.2%. At around 100 °C, the weight loss rate of the material is very fast, indicating that the material is mainly dehydrated at stage I. From 400 °C to 550 °C is the stage II of TGA curve, and the weight gains is 2.5%. At this stage, it is mainly the oxidation reaction of the material without generating gas. From 550 °C to 700 °C is the stage III of TGA curve, and the weight loss is 11.3%. The weight loss in stage III is mainly the decomposition of organic matter with generating gas. When heated above 700 °C, the weight of the material does not change, mainly due to changes in the crystallinity of the material.

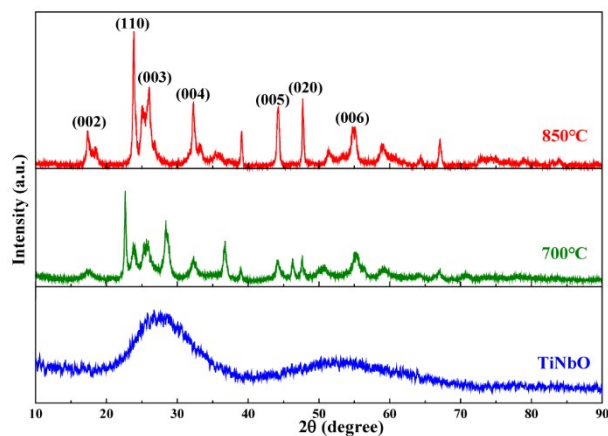


Fig. S3 XRD patterns of the titanium niobium oxide microspheres as a function of annealing temperature (from bottom to top: ambient temperature, 700 °C, and 850 °C).

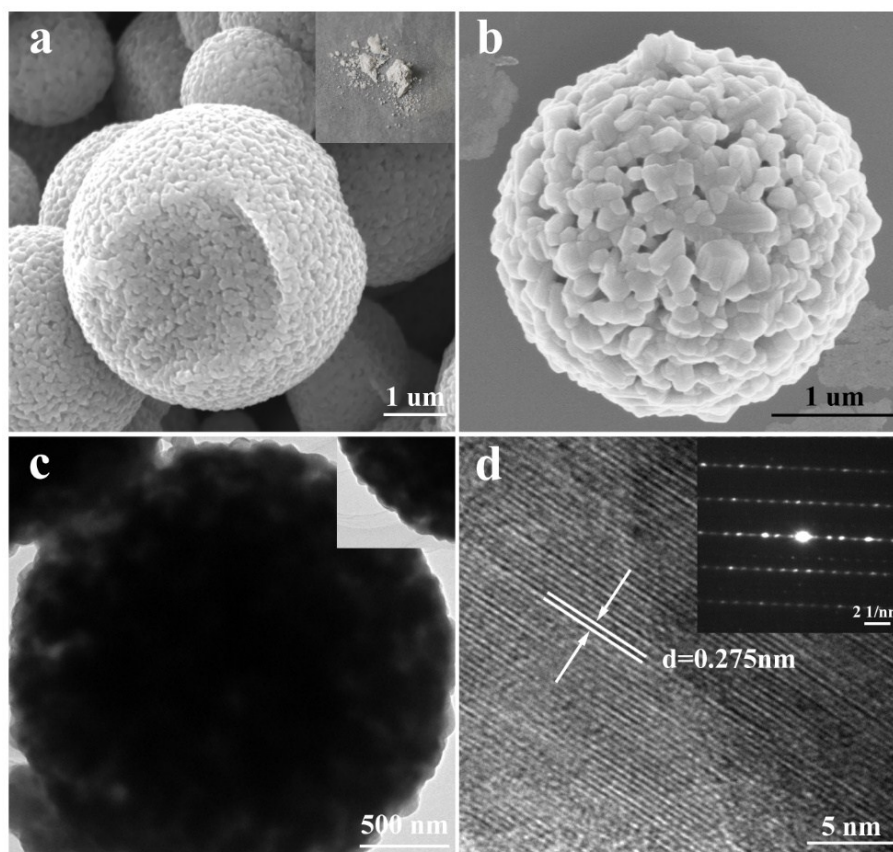


Fig. S4 (a-b) FESEM, (c) TEM and (d) HRTEM images of the porous TiNb_2O_7 microspheres after annealing. The inset of (a) is the photographs of the porous TiNb_2O_7 microspheres after annealing.

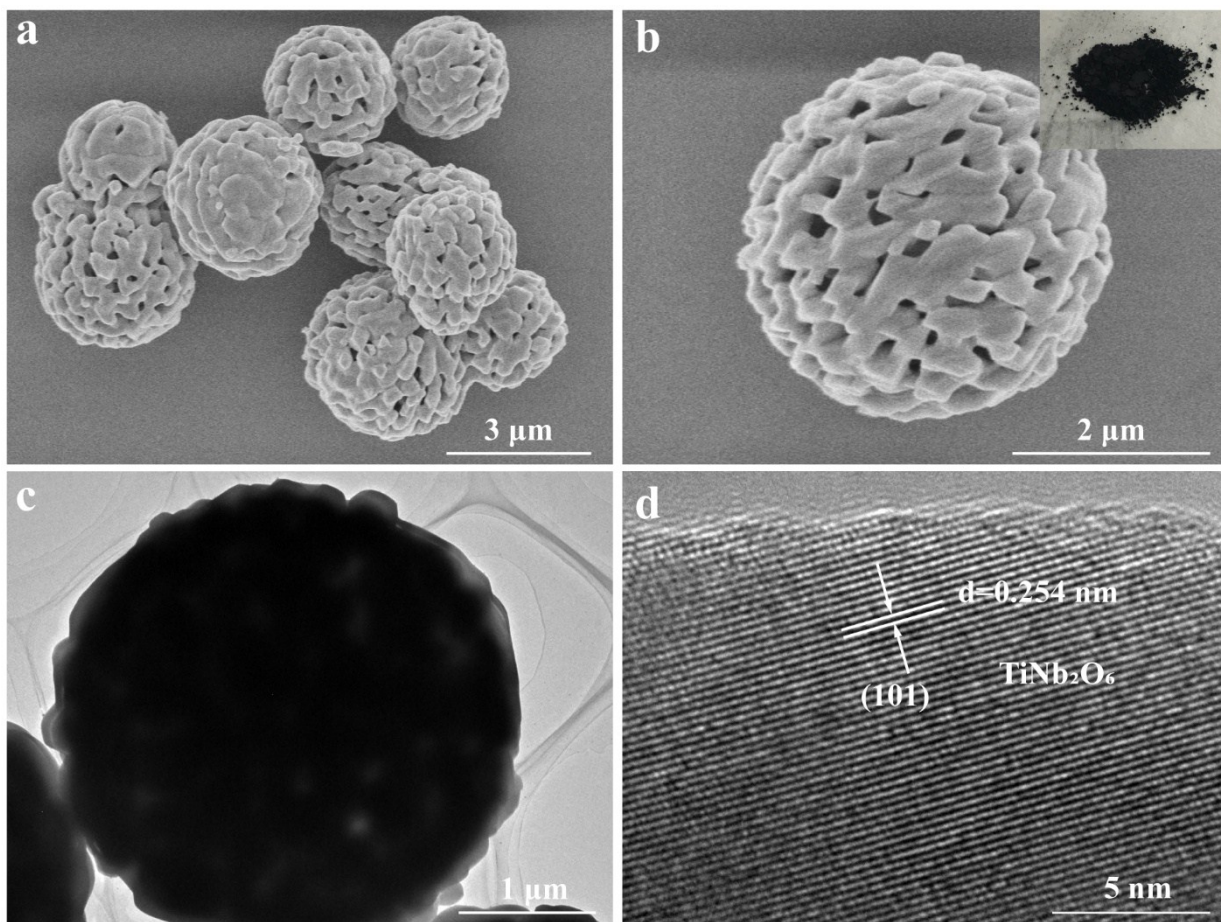


Fig. S5 (a-b) FESEM, (c) TEM and (d) HRTEM images of the porous TiNb_2O_6 microspheres after annealing. The inset of (b) is the photographs of the porous TiNb_2O_6 microspheres after annealing.

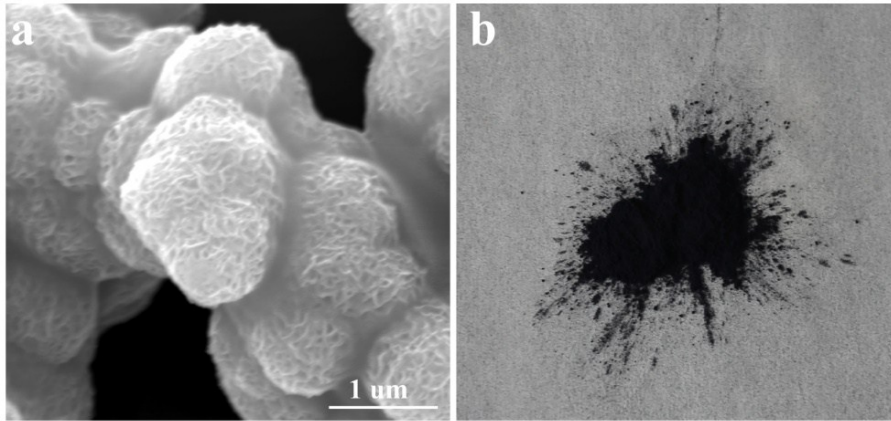


Fig. S6 (a) FESEM image and (b) the photograph of the porous $\text{TiNb}_2\text{O}_7@\text{MoS}_2/\text{C}$ microspheres before annealing in an $\text{Ar}/10\%\text{H}_2$ mixed atmosphere.

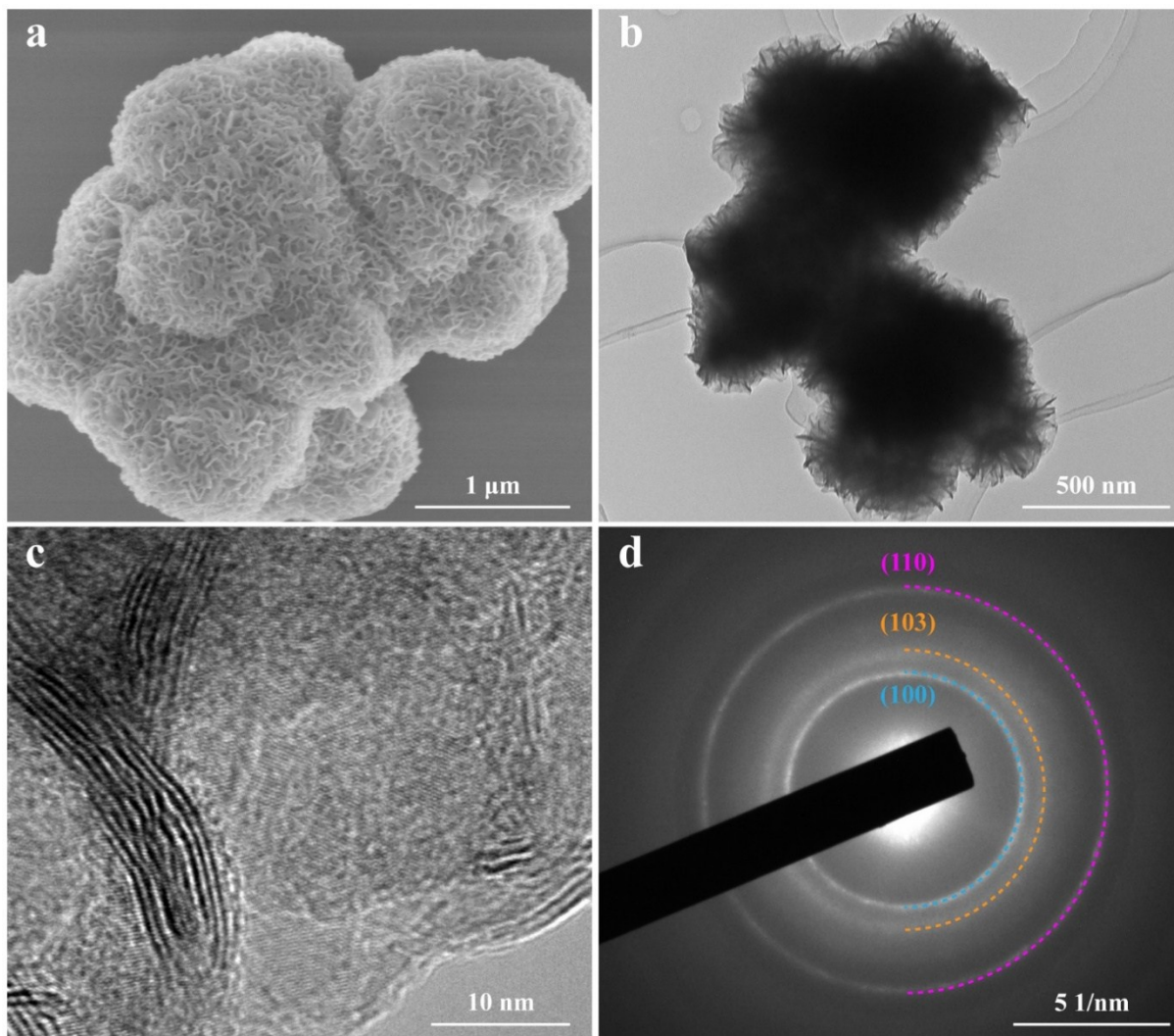


Fig. S7 (a) FESEM, (b) TEM, (c) HRTEM images and (d) SAED pattern of the MoS₂/C microspheres.

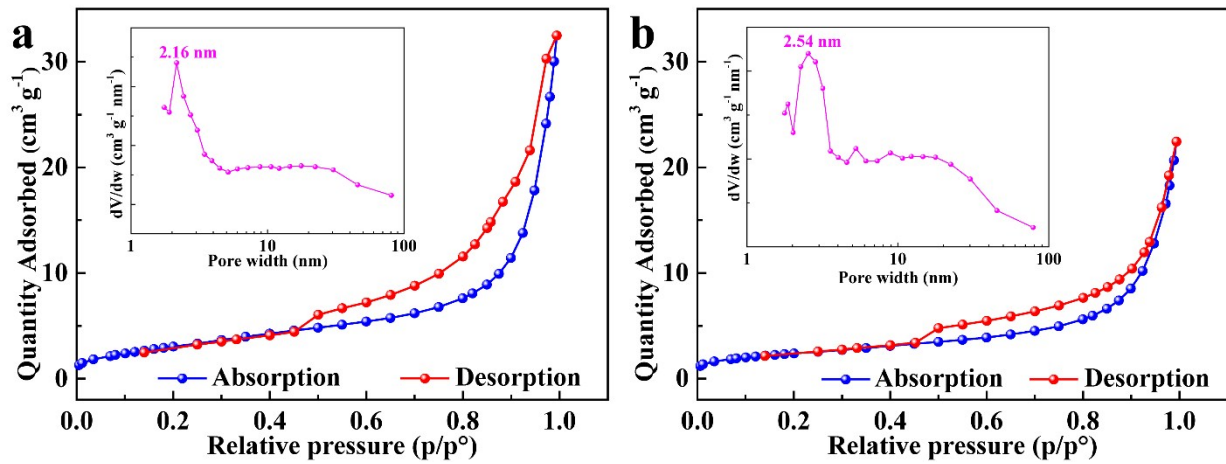


Fig. S8 Nitrogen adsorption-desorption isotherms of (a) $\text{TiNb}_2\text{O}_6@\text{MoS}_2/\text{C}$ and (b) MoS_2/C microspheres and the inset is pore size distribution.

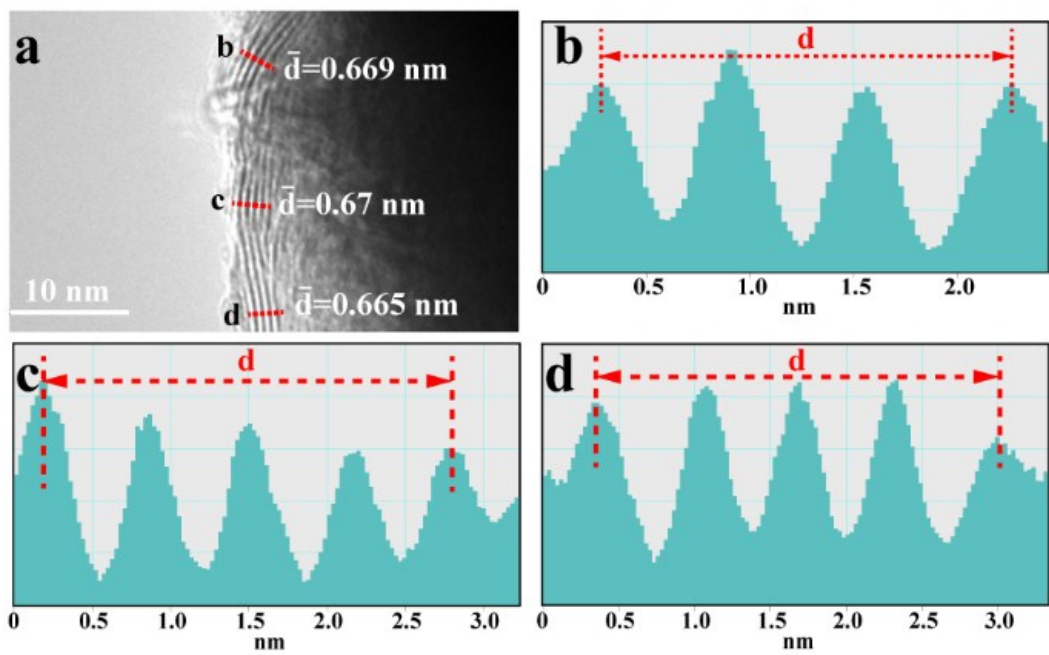


Fig. S9 (a) HRTEM image and (b-d) interlayer spacing measurement of the TiNb₂O₆@MoS₂/C hetero-structured microspheres.

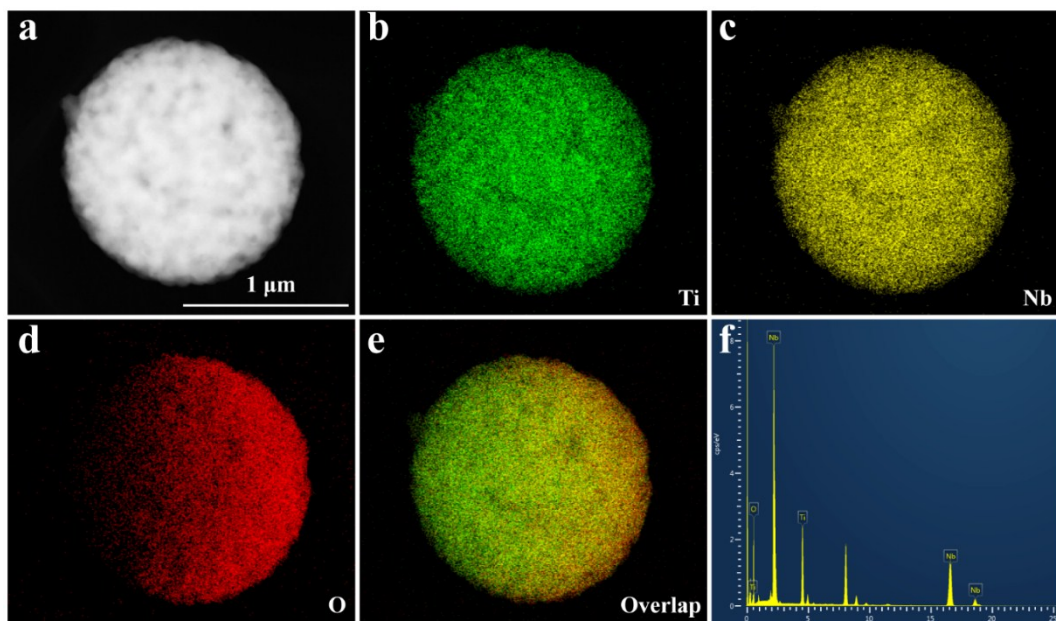


Fig. S10 (a) STEM image of porous TiNb₂O₇ microspheres; (b-e) The corresponding EDX elemental mapping images and (f) EDS pattern of porous TiNb₂O₇ microspheres.

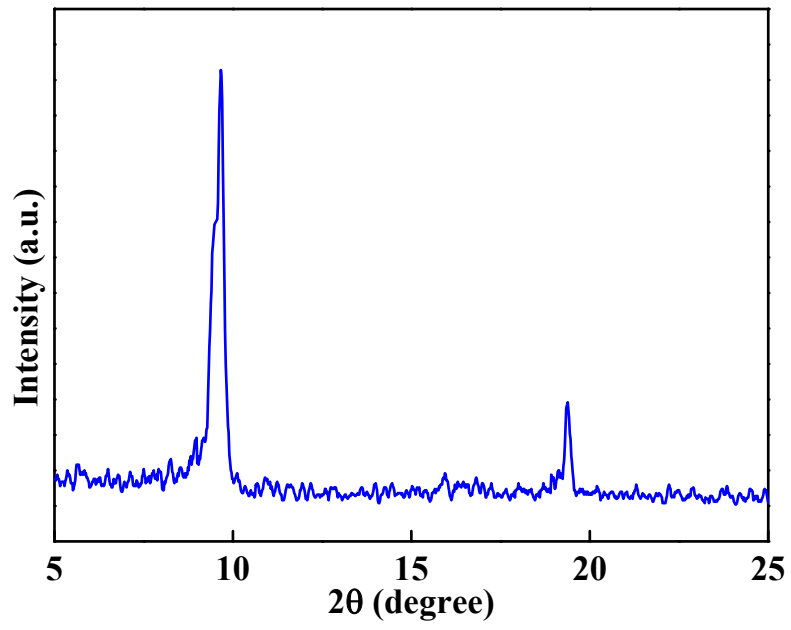


Fig. S11 XRD pattern of the MoS₂/C.

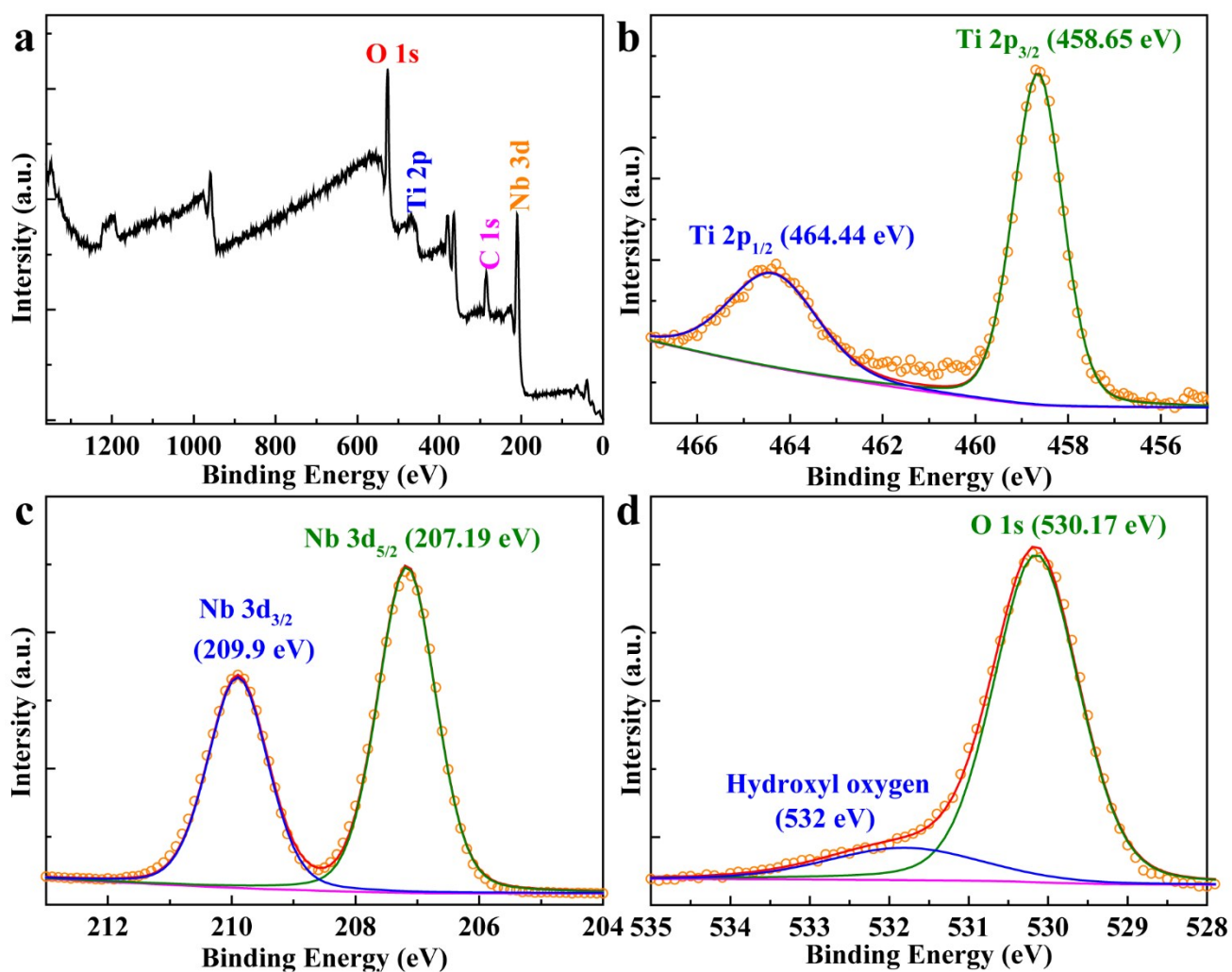


Fig. S12 XPS spectra of the TiNb₂O₇ microspheres: (a) survey scan and (b-d) high-resolution scans of Ti 2p, Nb 3d, and O 1s chemical bonding states.

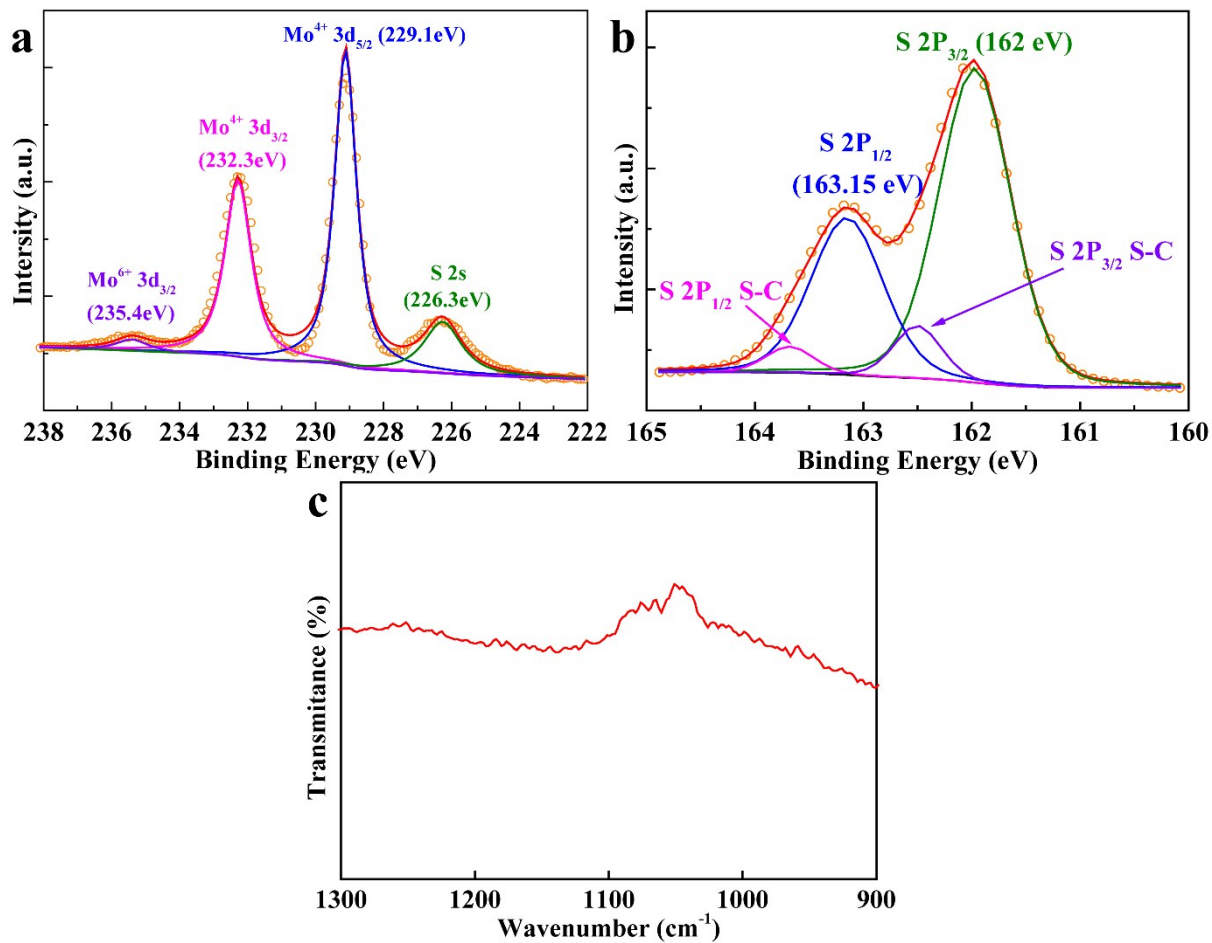


Fig. S13 XPS spectra of the MoS₂/C microspheres: high-resolution scans of (a) Mo 3d and (b) S 2p chemical bonding states. (c) IR spectra of the MoS₂/C.

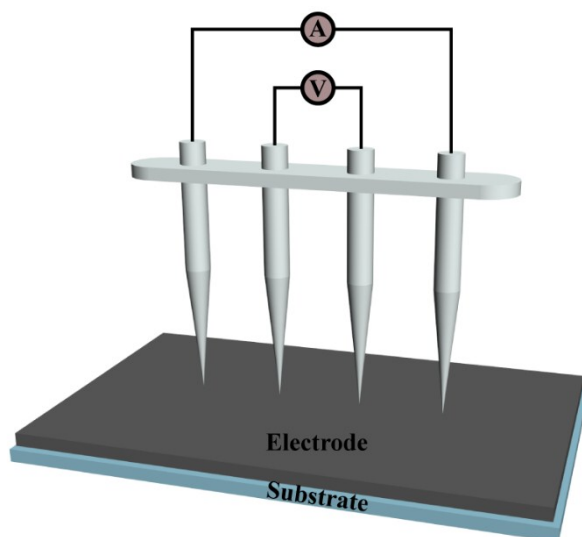


Fig. S14 Schematic illustration of the electronic conductivity measurements of the material films.

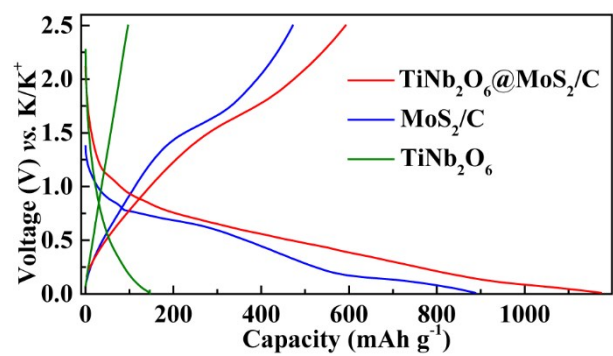


Fig. S15 The first charge/discharge curves of TiNb₂O₆-, MoS₂- and TiNb₂O₆@MoS₂-based anodes at a current density of 0.1 A g⁻¹ in the voltage range of 0.01–2.5 V.

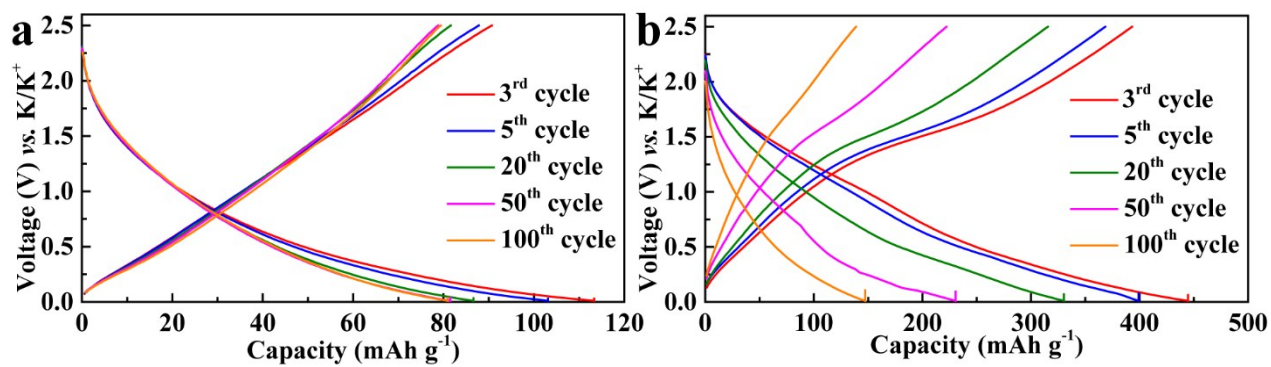


Fig. S16 (a-b) The charge/discharge curves of TiNb_2O_6 and MoS_2/C anodes at a current density of 0.1 A g^{-1} in the voltage range of $0.01\text{--}2.5 \text{ V}$.

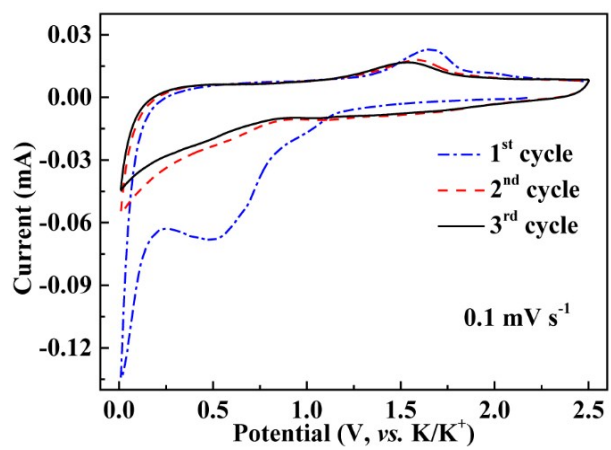


Fig. S17 CV curves from 1st to 3rd cycle at a scan rate of 0.1 mV s⁻¹.

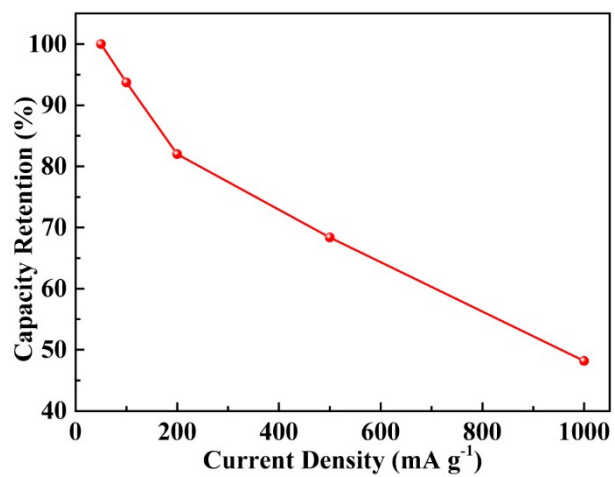


Fig. S18 The relationship between current density and capacity retention of TiNb₂O₆@MoS₂/C.

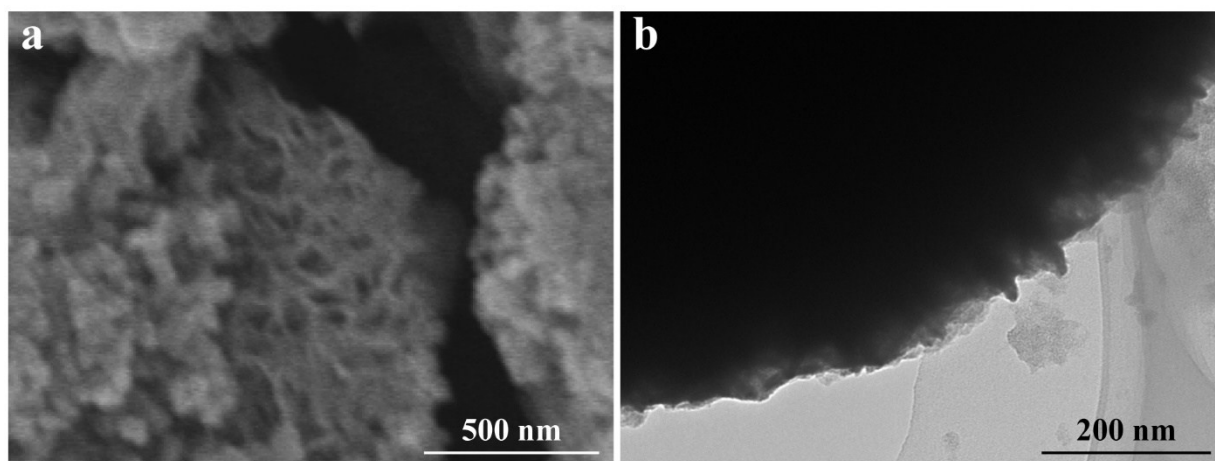


Fig. S19 (a) SEM and (b)TEM image of TiNb₂O₆@MoS₂/C electrodes after 300 cycles at 1.0 A g⁻¹.

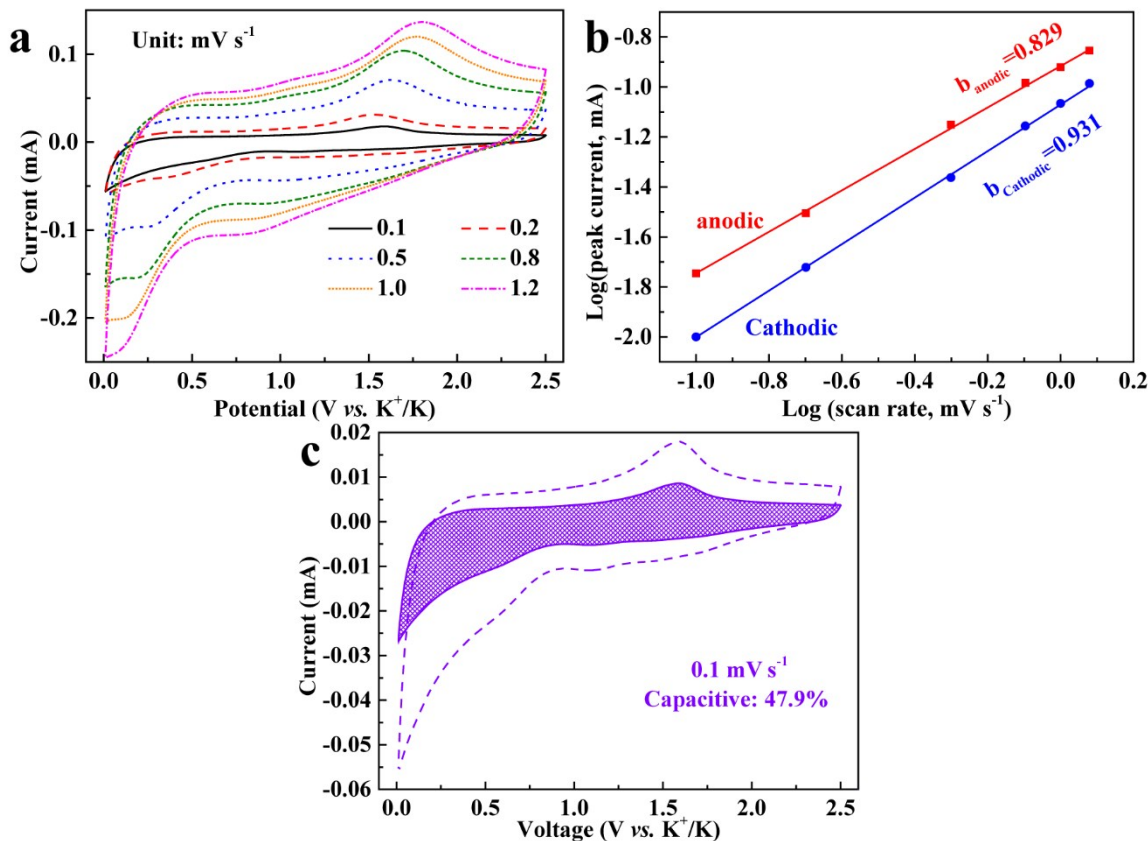


Fig. S20 (a) CV measurements of $\text{TiNb}_2\text{O}_6@\text{MoS}_2/\text{C}$ at various scan rates in the voltage range 0.01–2.5 V; (b) Cycling response of interconnected $\text{TiNb}_2\text{O}_6@\text{MoS}_2/\text{C}$ analyzed by the Randles-Sevcik equation; (c) Separation of the capacitive and diffusion-controlled charges at 0.1 mV s^{-1} .

To prove the capacitive behavior, the CVs are carried out at stepped scan rates from 0.1 to 1.2 mV s^{-1} in a voltage range from 0.01 to 2.5 V (Fig. S20a). According to the previous reports,¹ the peak current (i) and the scan rate (v) abide by the relationship of $i = av^b$. In the meantime, the b value can be obtained by the slope of the $\log(i)$ vs. $\log(v)$ plot (Fig. S20b). When the b value is close to 0.5 , the electrochemical behavior is dominated by the ionic diffusion process, while the b value close to 1.0 indicates a total capacitive process.² In this work, $b_{\text{anodic}} = 0.829$, $b_{\text{cathodic}} = 0.931$. The capacitive contribution ratio under different scan rates can be quantified through the Equation of $i = k_1v + k_2v^{1/2}$, where k_1v and $k_2v^{1/2}$ represent the contribution of capacitance and ionic diffusion, respectively.¹ When charging at a low scan rate of 0.1 mV s^{-1} , the b value is below 0.5 , indicating the charge storage behavior is dominated by the ionic diffusion process. To be specific, the values of K_1 and K_2 can be

obtained by fitting the coordinates of the redox peaks of different sweep speeds into the above formula.

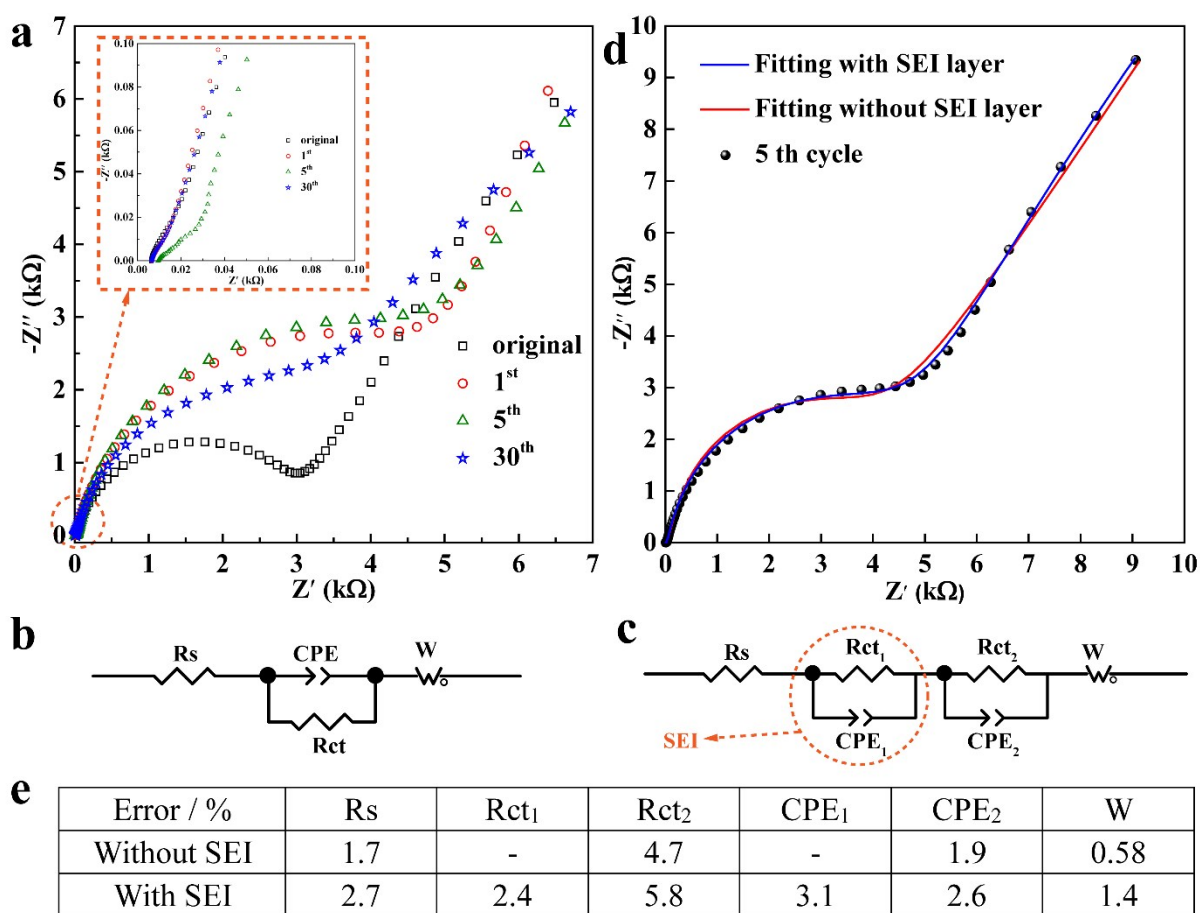


Fig. S21 (a) EIS plots and (b, c) equivalent electric circuit of the $TiNb_2O_6@MoS_2/C$ at different cycles. The result of (d) the fitting curve and (e) the corresponding error of the 5th cycle.

The EIS data were fitted by the equivalent circuit. R_s represents the internal resistance of the coin-cell battery and C_1 represents the capacitance. W_1 is associated with the Warburg impedance, corresponding to the potassium-diffusion process. R_{ct} and CPE are related to the charge-transfer resistance and the constant phase-angle element that involves double layer capacitance. In fact, the EIS curves can be divided into two semicircles, the semicircle at high frequency is caused by the SEI layer.

Table S1. The weight ratio of $\text{TiNb}_2\text{O}_6@\text{MoS}_2/\text{C}$.

Element symbol	Atomic ratio	Component	Weight ratio
Ti	1	TiNb_2O_6	1
Nb	1.9		
Mo	3.9	MoS_2	1.9
S	7.2		
C	7.4	C	0.3

The content of S and C can be tested by carbon sulfur analyzer. The content of Ti, Nb, Mo and S can be determined by ICP-OES. Finally, the composition of $\text{TiNb}_2\text{O}_6@\text{MoS}_2/\text{C}$ can be calculated from the results of ICP-OES and carbon sulfur analyzer. The test results show that the molar ratio of TiNb_2O_6 to MoS_2 is 1:3.9, which is very close to the ratio of 1:4.4 calculated on the basis of precursor.

Table S2 A comparison of the electronic conductivity of different materials.

Sample	Electronic conductivity (S m⁻¹)
TiNb₂O₆@MoS₂/C	492.6
TiNb₂O₇	101.4
MoS₂/C	140.4
TiNb₂O₆	1162

Table S3. Electrochemical performance survey of some reported anode materials of KIBs.

Sample	Current density (mA g⁻¹)	Capacity (mAh g⁻¹)	Cycle number	Reference
TiNb₂O₆@MoS₂/C	100	424	50	This work
	1000	175	300	
Hard Carbon	27.9	216	100	3
Soft Carbon	558	160	50	4
N-doped Graphene	100	210	100	5
N-doped Carbon	1000	152	3000	6
N/O-doped Carbon	1050	130	1100	7
C/Sn	50	280	100	8
Bi	800	322	300	9
Sn₄P₃/C	50	385	50	10
MoS₂@rGO	100	381	100	11
K₂Ti₈O₇	20	111	50	12
Sulfide/carbon	50	500	50	13
GeP₅	50	495	50	14

References

1. D. Su, A. McDonagh, S. Z. Qiao and G. Wang, *Adv. Mater.*, 2017, **29**.
2. J. Wang, H. Tang, L. Zhang, H. Ren, R. Yu, Q. Jin, J. Qi, D. Mao, M. Yang and Y. Wang, *Nat. Energy*, 2016, **1**, 16050.
3. Z. Jian, Z. Xing, C. Bommier, Z. Li and X. Ji, *Adv. Energy Mater.*, 2016, **6**, 1501874.
4. Z. Jian, W. Luo and X. Ji, *J. Am. Chem. Soc.*, 2015, **137**, 11566-11569.
5. K. Share, A. P. Cohn, R. Carter, B. Rogers and C. L. Pint, *ACS Nano*, 2016, DOI: 10.1021/acsnano.6b05998.
6. Y. Xie, Y. Chen, L. Liu, P. Tao, M. Fan, N. Xu, X. Shen and C. Yan, *Adv. Mater.*, 2017, **29**.
7. Y.-H. Zhu, X. Yang, D. Bao, X.-F. Bie, T. Sun, S. Wang, Y.-S. Jiang, X.-B. Zhang, J.-M. Yan and Q. Jiang, *Joule*, 2018, **2**, 736-746.
8. K. Huang, Z. Xing, L. Wang, X. Wu, W. Zhao, X. Qi, H. Wang and Z. Ju, *J. Mater. Chem. A*, 2018, **6**, 434-442.
9. K. Lei, C. Wang, L. Liu, Y. Luo, C. Mu, F. Li and J. Chen, *Angew. Chem. Int. Ed. Engl.*, 2018, **57**, 4687-4691.
10. W. Zhang, J. Mao, S. Li, Z. Chen and Z. Guo, *J. Am. Chem. Soc.*, 2017, **139**, 3316-3319.
11. K. Xie, K. Yuan, X. Li, W. Lu, C. Shen, C. Liang, R. Vajtai, P. Ajayan and B. Wei, *Small*, 2017, **13**.
12. J. Han, M. Xu, Y. Niu, G. N. Li, M. Wang, Y. Zhang, M. Jia and C. M. Li, *Chem. Commun.*, 2016, **52**, 11274-11276.
13. Y. Liu, Z. Tai, J. Zhang, W. K. Pang, Q. Zhang, H. Feng, K. Konstantinov, Z. Guo and H. K. Liu, *Nat. Commun.*, 2018, **9**, 3645.
14. W. Zhang, Z. Wu, J. Zhang, G. Liu, N.-H. Yang, R.-S. Liu, W. Pang, W. Li, Z. Guo, *Nano Energy*, 2018, **53**, 967-974.